Unconventional fabrication of 2D nanostructures and graphene edges

Bellunato, A.

Appendix I

Supporting Information to Chapter 3

I.I Materials and Methods

I.I.I The embedding polymer

The graphene edge electrode was embedded in a polymer scaffold made of pentaerythritol tetrakis (3-mercaptopropionate) (PEMPT; i.e., component A), and 1,3,5-Triallyl-1,3,5-triazine-2,4,6(1H,3H,5H)-trione (TATATO; i.e., component B) mixed in molar proportion 3 : 4 = A : B. The mixture was degassed under vacuum for about one hour. Next, 1%$_{WT}$ of dimethoxy-phenylacetophenone was added to the A : B mixture as photo-initiator[1,2]. Last, the polymer was hardened in air under the irradiation of a 365 nm ultraviolet lamp for 30 minutes, 7000 μW/cm^2 at 38,2 cm of distance.

I.I.II Preparation of the graphene layer

A drop of polymer was casted and cured onto a Si/SiO_2 wafer (purchased from University Wafer) patterned with a thermally evaporated gold electrode (5 X 5 mm^2, homemade thermal resistance evaporator operating below 1x10^{-6} bar). The embedding polymer contains thiol functionalities, promoting a strong adhesion to the gold. Next, to lift the gold electrode from the SiO_2 surface, a razor blade is intercalated between the polymer and the surface of the wafer. The lift-off process yields an ultra-flat polymeric substrate embedding a gold contact pad used for the electrical connection of the graphene sample. The cured polymer embedding the gold electrode was then exposed to an oxygen plasma (Diener Plasma Etcher at 0.3mbar O_2, 60W for 30s) in order to convert its surface to hydrophilic. Afterwards, the polymeric substrate was immersed in a petri-dish containing ultra pure water with the gold electrode facing the water surface. Subsequently, a graphene layer coated with poly (methyl methacrylate), PMMA, was transferred floating over the water surface. The transfer proceeds via the removal of the water and the gentle deposition of the graphene over the surface of the polymer across the gold electrode. The alignment of the PMMA coated graphene with the gold electrode was performed using a needle and a micro-manipulator. Graphene was purchased from Graphenea®, grown via chemical vapor deposition on top of a Cu substrate. The graphene layer was spin-coated with PMMA and back-etched using an oxygen plasma at 0.3 mbar O_2, 60 W for 45 s, in order to remove any trace of carbon from the uncoated (back) side of the Cu substrate. Afterwards the Cu was etched in a

0.5 M solution of $(NH_4)_2S_2O_8$. Following the etching of the copper, the PMMA coated graphene was rinsed through three petri-dishes filled with ultra pure water, in order to remove any trace of etchant from the surface of the graphene. All the chemicals were purchased from Sigma-Aldrich®.

I.II Microtomy

The edge electrode was exposed through the polymer scaffold by microtomy sectioning (see Figure 3.1 of Chapter 3). The polymeric matrix embedding the edge of graphene was first cut in two parts with a razor blade in order to expose the graphene. Next, the surface of the polymer scaffold exposing the graphene edge was flattened by trimming via microtomy employing a Leica® EM UC 6 mounting a Diatome® trim tool 20®. Last, the polymer scaffold was finely sectioned by microtomy using an Ultra Diamond Knife 35®. The microtomy process yields an ultra-flat polymeric surface exposing the edge of a PMMA-coated graphene film, namely the graphene edge electrode (see Figure 3.1 of Chapter 3).

I.III Cyclic voltammetry

The graphene edge acts as a working electrode in a two electrodes system against an Ag/AgCl reference/counter electrode. Cyclic voltammetry characterizations were performed using an Autolab® potentiostat. The characterization of the edge was performed initially in 0.1 M KCl at 0.1 Vs^{-1}, 0.05 Vs^{-1} and 0.01 Vs^{-1}. The cyclic voltammetry in presence of a redox probe was performed at 0.05 Vs^{-1} with a 5 mM solution of $K_3Fe(CN)_6$ in 0.1 M KCl. The functionalization with a nitrobenzene tetrafluoroborate diazonium salt, $BF_4N_2C_6H_4NO_2$, was carried in a solution of 1 mM $BF_4N_2C_6H_4NO_2$ in 0.1 M $HClO_4$ in ultra pure water. All the chemicals were purchased from Sigma-Aldrich®.

I.IV Raman characterization

The graphene was first characterized by Raman spectroscopy on top of a Si/SiO_2 wafer (inset Figure 3.2a of Chapter 3). A sample of PMMA coated graphene was transferred over a SiO_2 substrate. Next, the PMMA was removed with acetone and the sample was rinsed with isopropanol and ethanol.

Additionally, the variation of the Raman signature of the embedding polymer was monitored to exclude the adsorption of nitrobenzene on the polymeric surface. The edge electrode and the surrounding polymer were rinsed with ultra pure water after electrografting. Figure I.1 shows the Raman spectroscopy of the embedding polymer before (black curve) and after (red curve) functionalization of the edge electrode. No significant changes in the Raman spectra occurred after the electrografting reaction (particularly observing the peaks at 1425 cm^{-1} and 1650 cm^{-1}), indicating that the electrografting did not involve the polymer embedding (only the edge electrode as discussed in Chapter 3).

All the Raman spectra were acquired using a WITec Raman Alpha 3000® instrument equipped with a 532nm laser source.

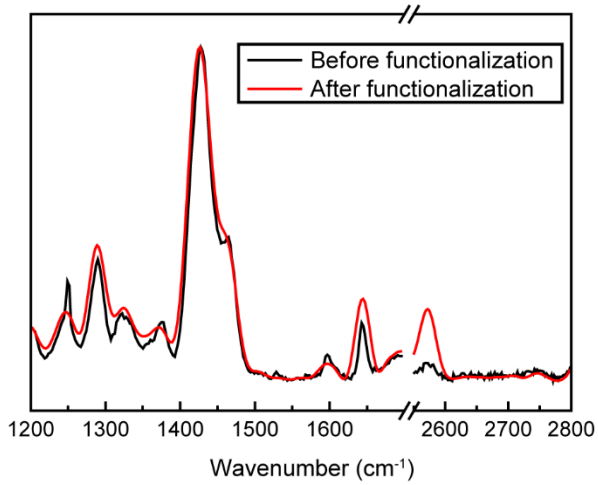

Figure I.1. Raman spectra of the embedding polymer. Black curve: Raman spectrum obtained with a 532 nm laser before the electrografting reaction. Red curve: Raman spectrum obtained with a 532 nm laser after the electrografting reaction. The spectra are normalized over the peak at 1425 cm^{-1}.

I.V Electrical characterization

The gating experiments were performed using a lock-in amplifier from Stanford Research System (SR830). The electrical characterization of the graphene transistor was performed in a liquid gating configuration (see Figure 3.5 of Chapter 3 and Figure I.2a). The graphene edge electrode was loaded at the gate voltage through a 1 M KCl solution and an Ag/AgCl electrode connected to the direct

coupling (DC) source of the amplifier, sweeping the gating potential between -0.5 V and 0.2 V.

The output voltage of the lock-in was set at 1 V and 77.77 Hz and connected to a 1 MΩ resistor used to impose a 1 µA current through the source and drain of the transistor, while the drain was grounded (Figure 3.5 of Chapter 3 and black line connecting the gold electrodes in the schematics of Figure I.2a).

The edge selectivity of the electrografting was confirmed with a control experiment forming an edge on SiO_2 via oxygen plasma etching. Figure I.2a shows the preparation of the sample: a CVD film of graphene was deposited on a SiO_2 substrate and partially covered with the PEMPT-TATATO polymer. The excess of graphene was etched using an oxygen plasma. The remaining graphene was covered by the polymer. The role of the polymer is to protect the graphene, forming an edge at its extremity. Next, the graphene was probed electrically using a liquid gating configuration as shown in Figure I.2a (right side) using a 1 M KCl electrolytic solution.

Afterwards, the edge was first functionalized by electrografting nitrobenzene diazonium via cyclic voltammetry with voltages ranging from 0.05 Vs^{-1} to -0.5 V and 0.1 V in a 1 mM solution of 4-nitrobenzene diazonium tetrafluoroborate (NBD; $BF_4N_2C_6H_4NO_2$) dissolved in an acidic solution of 0.1 M perchloric acid ($HClO_4$), and then probed electrically.

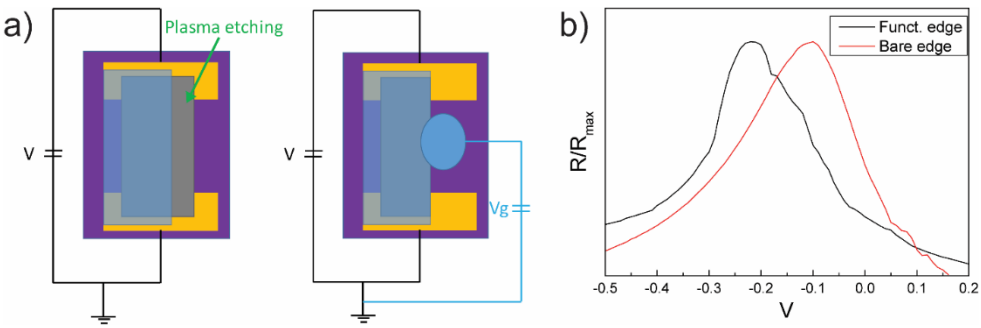

Figure I.2. Graphene edge electrode fabricated on a Si/SiO_2 wafer. a) A graphene field effect transistor, GFET, with an exposed edge electrode was formed by partially coating a graphene film with the PEMPT/TATATO polymer. An oxygen plasma etches the unprotected graphene, forming an edge at the interface with the protecting polymer. The edge electrode was in contact with an electrolyte solution of 1 M KCl and a gate potential

V_g was applied to the edge through the solution. b) Conductivity measurements of the GFET before functionalization (red curve) and after functionalization (black curve).

Figure I.2b compares the gating curves of the graphene film before functionalization (red curve) and after functionalization (black curve). The results of the control experiment in Figure I.2b suggest a behaviour comparable to what was observed with the polymer-embedded graphene edge electrode in Figure 3.3d in Chapter 3. As shown in Figure I.2b, the conductivity of the graphene sample was negligibly affected by the electrografting at the edge, indicating the protection of the basal plane towards electrografting. The shift in resistivity at the charge neutrality point was around three times the minimum in resistivity at negative gating potential, as observed also for the edge electrode in Chapter 3.

I.VI References

(1) Lu, H.; Carioscia, J. A.; Stansbury, J. W.; Bowman, C. N. *Dent. Mater.* **2005**, *21* (12), 1129–1136.

(2) Mays, R. L.; Pourhossein, P.; Savithri, D.; Genzer, J.; Chiechi, R. C.; Dickey, M. D. *J. Mater. Chem. C* **2013**, *1* (1), 121–130.

Appendix II

Supporting Information to Chapter 4

II.I Materials and Methods

II.I.I Graphene

Graphene nanogaps were formed using chemically vapor deposited graphene, CVD, on Cu purchased from Graphenea®. Before the deposition on the supports, the copper substrate of the CVD graphene was removed via wet etching in a 0.5 M aqueous solution of ammonium persulfate $(NH_4)_2S_2O_8$ purchased from Sigma-Aldrich®.

II.I.II The protecting polymer

Graphene was first coated with a protecting film of poly (bisphenol A carbonate), PCA (M_W 45000 $gmol^{-1}$), prepared in a chloroform solution (1.5% wt). The film was spin-coated at 4000 rpm for 60 s over the graphene film on copper. After the deposition on the Si/SiO_2 substrates, the suspended graphene was etched via reactive ion etching. Afterwards, the protecting PCA film was dissolved in chloroform overnight and rinsed in methanol and isopropanol (all the chemicals were purchased from Sigma-Aldrich®).

II.I.III Preparation of the supports

The graphene edge electrodes were prepared by etching of a suspended graphene film transferred over two independent Si/SiO_2 supports.

We employed undoped Si/SiO_2 supports from Sieger Wafers® with a polished oxide surface 285 nm thick. The supports were prepared by notching a Si/SiO_2 wafer using a diamond scribe. The notch indents the oxide initiating a crack in the Si crystal. Upon applying strain to the wafer, the crack propagates along the crystallographic orientation of the wafer yielding two supports with extremely sharp edges. Sharp edges were a prerequisite to have uniform edge electrodes and facilitate the approach of the tunnelling junction.

Before the deposition, the supports were cleaned by organic solvents (acetone, isopropanol, ethanol) and further cleaned in a piranha solution (1:3=hydrogen peroxide : sulphuric acid) and afterwards exposed to O_2 plasma at 0.3 mbar 60 W for several minutes. The piranha solution and the plasma clean the surface of the

Si/SiO_2 wafers from any organic residuals, increasing the hydrophilicity of the surface to facilitate the deposition of the graphene.

II.I.IV Plasma etching

The etching of the suspended graphene and the formation of the independent edge electrodes employed to form the tunnelling junction was performed using a Diener GmbH plasma etcher.

II.I.V Sheet resistance and point contact resistance

In contrast to 3D metallic systems, the point contact resistance measured here was dominated by a large contribution from the sheet resistance of the graphene electrodes that cannot be separated from the measurements. The total measured resistance was the quantum point contact resistance in series with the classical resistance of the sheets. The classical resistance R_G of the sheets on either side of the contact can be estimated as (1):

$$R_G = \frac{1}{\pi\sigma}\int_{l_0}^{L}\frac{1}{r}dr \quad (1)$$

where σ is the sheet conductance, L is the size of the sample (2mm), and l_0 is the electrons mean free path. Using the semi-classical expression for the sheet conductance (2):

$$\sigma = \frac{e^2}{h}2E_F\tau/\hbar \quad (2)$$

and the linear dispersion of the Fermi energy $E_F = \hbar v_F k_F$, and $k_F = \sqrt{\pi n}$, we can express the mean free path in terms of the conductivity and the electron density (3):

$$l_0 = \frac{\sigma}{e^2/h}\frac{1}{2\sqrt{\pi n}} \quad (3)$$

Using the conductance of $\sigma = (11 \pm 2)\, e^2 / h$ found for our samples, and the typical dependence between charge density and conductance in this regime[1,2] we obtained an estimate of $l_0 = 27$ nm. With this, an estimated resistance for the sum of the two graphene electrodes of $17 \pm 3\ \mathrm{k\Omega}$ was obtained. Subtracting twice this value from the measured point contact resistance of 28 kΩ, we found an estimate for the quantum point contact resistance of 11±3 kΩ.

II.I.VI Simmons model for symmetric barrier

Considering tunnelling through a symmetric barrier, the work function ϕ can be approximately the same for both electrodes. The current density in a symmetric tunnel junction with a barrier along the z-axis (Figure II.1) is described with a Simmons model[3] (4):

$$J \sim \frac{e}{2\pi h d^2}\left[(\phi - \mu_L)e^{-\frac{2d\sqrt{2m(\phi-\mu_L)}}{\hbar}} - (\phi - \mu_R)e^{-\frac{2d\sqrt{2m(\phi-\mu_R)}}{\hbar}}\right] \quad (4)$$

where $d = z_1 - z_2$, and μ_L and μ_R are the chemical potentials of the left and the right electrode, respectively.

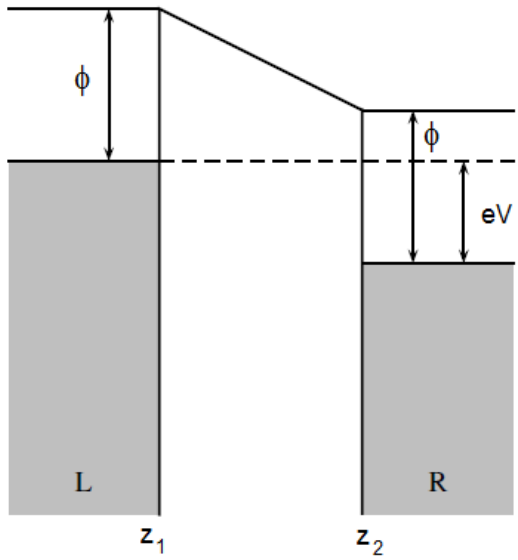

Figure II.1. Symmetric tunnel junction with barrier height ϕ and barrier width $d = z_1 - z_2$

Parameters fitted to the Simmons model are the pre-factor *A* (which contains a cross-section of the junction), the barrier height φ and the gap size *d*. The parameters *A* and φ cannot be fitted completely independently, but with a suitable choice for the pre-factor the barrier height obtained agrees with the range of results found in the literature, see the main text. The gap distance *d* is more robust and it is estimated with approximately 5% accuracy.

II.II Graphene-gold tunnelling junction

In order to identify the edge electrodes that extend to the end of their supports, we formed a tunnelling junction against a gold sample. This, in first instance allowed the facile electrical characterization of the edge electrode and secondly demonstrated the flexibility of our system, capable of employing independent edge electrodes in multiple systems, either symmetric or asymmetric junctions.

Figure II.2a illustrates the schematics of the set-up. The graphene edge electrode was mounted on a holder over a piezoelectric actuator (thick grey block on the left) which approaches a thick sample of pure gold. Figure II.2b shows the I(V) characteristic of the tunnel junction at a fixed distance, sweeping the bias voltage V between -1.5 V and + 1.5 V. The shape of the sigmoidal IV curve is characteristic of an asymmetric tunnel barrier. This is a result of the different work function across the two terminals of the junction. Figure II.2c shows the tunnelling current as a function of distance (black curve, *I(z)*) between the graphene and the gold sample at $V = 0.48$ V bias voltage. A clear exponential increase (exponential fit red curve) of the current with decreased distance was observed, characteristic of a tunnelling regime.

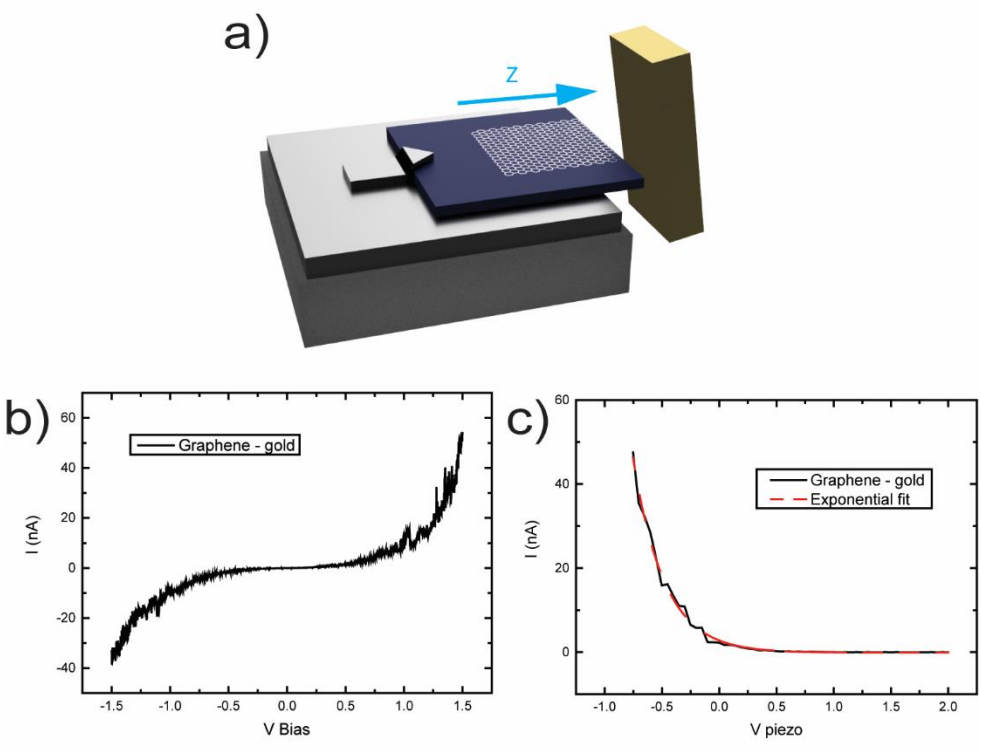

Figure II.2. a) Schematics of the gold – graphene tunnel junction etched in H_2 plasma. The graphene electrode was mounted on a piezoelectric actuator which moves the sample along the Z axis to approach a gold macro electrode. b) IV characteristic of the graphene-gold junction. c) Representative I(z) characteristic of graphene-gold tunnel junction (black line) fitted to exponential function (red line).

II.III Oxygen and nitrogen etching

Reactive ions etch the suspended graphene until the edge of the SiO_2 supports. The etching atmosphere, consequently, affects the chemistry of the graphene edge electrodes. In order to study the effect of different chemistries on the characteristics of the edge electrodes, we performed etching in various plasma atmospheres, namely: H_2, O_2 and NH_3.

The results concerning etching in hydrogen plasma are reported in the main text of Chapter 4, illustrating the successful formation of independent supported graphene edge electrodes. The same etching conditions (0.3mbar at 60W, 30s) were applied for O_2 and NH_3, etching the suspended graphene. While these

conditions worked for a hydrogen atmosphere, we did not manage to build stable tunnelling junctions between two graphene edge electrodes using O_2 and NH_3 plasmas. Particularly, no tunnelling devices were obtained with NH_3 etching, while stable asymmetric junctions were achieved using graphene edge electrodes prepared in O_2 plasma when measured in tunnelling junctions against gold counter-electrode, Figure II.3. The asymmetric IV characteristic confirmed the tunnelling between carbon and gold electrodes, but it was not possible to extrapolate the correct value of the work function and thus the tunnelling gap size, primarily because of the impossibility of fitting the results with the Simmon's model, Figure II.3a. The current-distance, I(z), characteristic was noisier and appeared less stable than the ones obtained with hydrogen. Once more, the lack of information about the work-function did not allow to calibrate the distance between the edge electrode and the gold counter electrode. Nonetheless, an exponential increase of the current was still observed at tunnelling current, Figure II.3b.

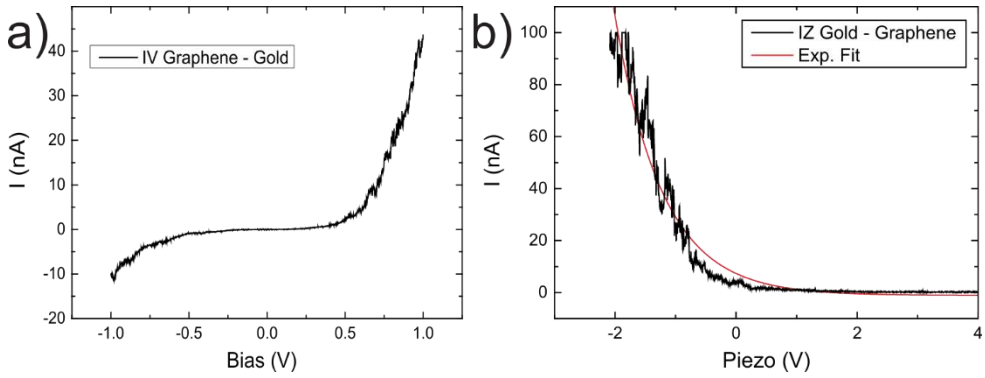

Figure II.3. Graphene – gold tunnelling junctions etched in an oxygen plasma. a) I(V) characteristic of the junction. b) I(z) characteristic of the tunnelling junction showing current exponential growth while approaching the gold counter electrode.

Comparing Figure II.2b and Figure II.3a a slight delay on the inset of the tunnelling currents for hydrogenated edges (Figure II.2b) can be observed with respect to the bias voltage for oxygen etched edge electrodes (Figure II.3a). Nonetheless, the lack of information due to the impossibility of fitting the Simmon's model, did not allow the proper calibration of the piezo stage. However, the qualitative differences

acting on different edge chemistries can be explained. We observed a strong asymmetricity in the case of oxygen etched electrodes. Particularly, for the same bias voltage in the IV curve of Figure II.3a compared to Figure II.2b, we can observe a higher tunnelling current at positive bias potentials, and lower at negative. If the difference at positive potentials could be ascribed to a closer distance of the gap in the case of oxygenated edges with respect to hydrogenated edges, this does not justify the lower current intensity at negative potentials. A possible explanation is the differences in the work functions between oxygenated and hydrogenated edges. The work function works as a barrier for tunnelling electrons. Smaller work functions are expected for hydrogenated edges, which at negative bias voltages might represent a smaller tunnelling barrier with respect to oxygenated edges, thus increasing the transmission intensity from graphene to gold electrodes. Accordingly, the tunnelling intensity at negative bias potentials was lower for oxygenated edges (higher barrier) than for hydrogenated edges (lower barrier), possibly showcasing the effect of the edge chemistry on the electron transmission through the tunnelling junction.

II.IV References

(1) Hwang, E. H.; Adam, S.; Sarma, S. Das. *Phys. Rev. Lett.* **2007**, *98* (18), 186806.

(2) Novoselov, K. S.; Geim, A. K.; Morozov, S. V.; Jiang, D.; Katsnelson, M. I.; Grigorieva, I. V.; Dubonos, S. V.; Firsov, A. A. *Nature* **2005**, *438* (7065), 197–200.

(3) Simmons, J. G. *J. Appl. Phys.* **1963**, *34* (6), 1793–1803.

Appendix III

Supporting Information to Chapter 5

III.I Materials and methods

III.I.I Graphene

Graphene nanoribbons were formed using chemically vapor deposited, CVD, on Cu purchased from Graphenea®. Graphene sheets were deposited on Si/SiO_2 wafers (285 nm thick SiO_2 purchased from University Wafer) and on gold coated mica substrates purchased from Ted-Pella®. The copper substrate of the CVD graphene was previously etched using a 0.5 M aqueous solution of ammonium persulfate $(NH_4)_2S_2O_8$ purchased from Sigma-Aldrich®.

III.I.II The metallic mask

Graphene nanoribbons were fabricated underneath metallic masks prepared via microtomy of metallic thin films embedded in a polymer scaffold. The metallic thin films were first thermally evaporated (Leiden University home built thermal resistance evaporator operating below $1x10^{-6}$ bar) on a Si/SiO_2 wafer (purchased from University Wafer), then coated with a drop of photocurable polymer (see Appendix I.I.I) and cured. The metallic films were lifted from the SiO_2 substrate using a razor blade intercalated between the metallic film and the surface of the wafer. Next, the metallic film coated with a polymer drop was immersed in a mould filled with photocurable polymer and cured, yielding a metallic thin film embedded in a polymer scaffold (Figure 5.1 of Chapter 5). The polymer scaffold is sectioned using a Leica® EM UC 6 microtome equipped with a Diatome® trim tool 20® and an Ultra Diamond Knife 35®, yielding polymeric slabs embedding metallic nanorods and with a surface ranging from 50 X 50 μm^2 to 150 X 150 μm^2 and from 50 nm to 150 nm thick, using a cutting speed varying between 1,0 mms^{-1} and 2,5 mms^{-1}.

III.I.III Plasma etching

The polymer slab and the excess of graphene were etched in O_2, H_2 and NH_3 using a Diener Electronic GmbH plasma etcher according to the experimental conditions reported in Chapter 5.

III.II Square resistance of graphene

Square resistance, or sheet resistance, is a unit of resistance employed in thin films of known uniform thickness, such as monoatomic graphene. Starting from the conventional definition of resistance R (1):

$$R = \rho \frac{L}{A} = \rho \frac{L}{WT} \quad (1)$$

The square resistance was derived applying the know thickness, T, of the film as a constant, thus in the case of graphene T=0.34 nm and (1) became (2):

$$R = \rho' \frac{L}{W} \quad (2)$$

Both sheet length, L, and width, W, were expressed in m, thus R returned a value in Ohm. The special case where R = ρ' represents the case where W = L, thus a square. Practically, the resistivity of the graphene film could be measured where W = L taking the name of square resistance R=(ohm/sq.).

In the case of graphene, the square resistance varies greatly according to experimental conditions, particularly the temperature, the nature of the electrical contacts and the substrate roughness. Nonetheless, the literature reported graphene square resistances in the order of hundreds of Ohm/sq[1,2], with an average around 600 Ohm/sq. Graphene purchased from Graphenea®, as the one employed in the experiments, reports an average of 450 Ohm/sq. on SiO_2. (https://www.graphenea.com/products/monolayer-graphene-on-sio2-si-4-wafer) in line with the values obtained for our measurements, i.e. R =1.65 kΩ for a device 80nm wide and in the order of 1 μm long.

III.III Electron beam lithography of metallic electrodes

In order to characterize electrically the graphene nanoribbons formed underneath the metallic mask, electrodes were deposited also via electron beam lithography (Raith® eLine electron beam pattern generator, EBPG). Nonetheless, by means of EBPG lithography we could not properly form electrodes. A first major issue was the difficult alignment between the nanometre wide graphene nanoribbons and the electron beam of the EBPG, yielding misplaced electrodes with respect to the nanostructures, Figure III.1a.

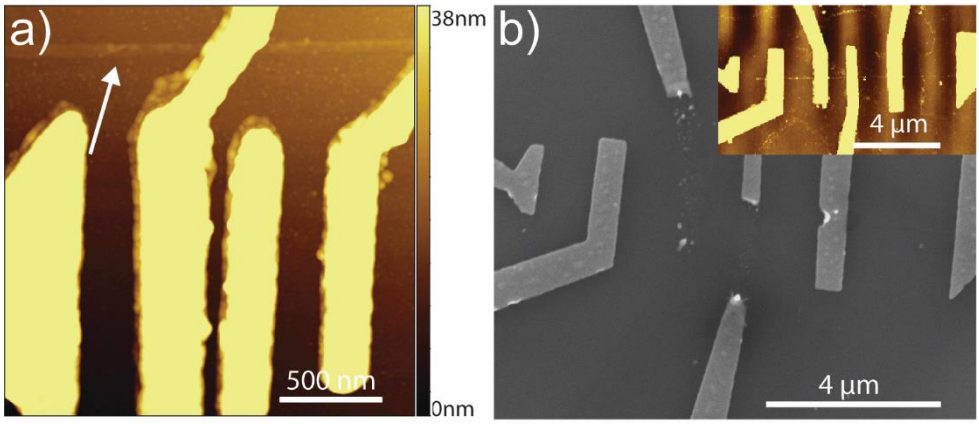

Figure III.1 AFM and SEM micrographs of gold electrodes prepared by electron beam lithography. a) AFM micrograph of gold electrodes misaligned with respect to a graphene nanoribbon. Bright yellow: gold electrodes designed via EBPG. The graphene nanoribbon, bright line on top highlighted by the white arrow, does not cross all the electrodes due to misalignment issues. b) SEM micrograph of electrodes broken during electrical characterization by means of electrons discharge. Inset: AFM micrograph of the graphene nanoribbon and the correctly aligned electrodes before electrical characterization.

Second, electrodes designed via electron beam lithography EBPG (even if correctly aligned over the graphene nanoribbon) showed severe discharging issues during the electrical characterization of the graphene nanoribbons leading to their rupture, Figure III.1b. More in detail, the inset of Figure III.1b shows the atomic force microscope AFM image of gold electrodes (bright yellow lines) crossing a graphene nanoribbon before the electrical characterization. Upon electrical characterization, an electronic discharge caused the rupture of the electrodes, as illustrated by the scanning electron microscope, SEM, micrograph in Figure III.1b. Because charges accumulate on the sample during EBPG, the electrical characterization forms a closed circuit with the sample, allowing the sudden flow of these accumulated charges, enabling a current flows which intensity is high enough to damage the electrodes.

III.IV Scalability

Metallic masks were prepared via microtomy of metallic thin films. Microtomy finely fabricated masks of different widths. The top panels of Figure III.2a to III.2c show metallic nanorods of different widths prepared via microtomy and used to form graphene nanoribbons, bottom panels of Figure III.2a to III.2c.

Importantly, the graphene nanoribbons were all prepared under the same etching conditions in H_2 plasma at 0.3 mbar 60 W for 2.5 minutes in order to remove the polymer slabs supporting the nanorods and the excess of graphene. The partial diffusion of reactive ions underneath the metallic masks yielded nanoribbons thinner than the mask and scaling with the mask width, Figure III.2d and III.2e.

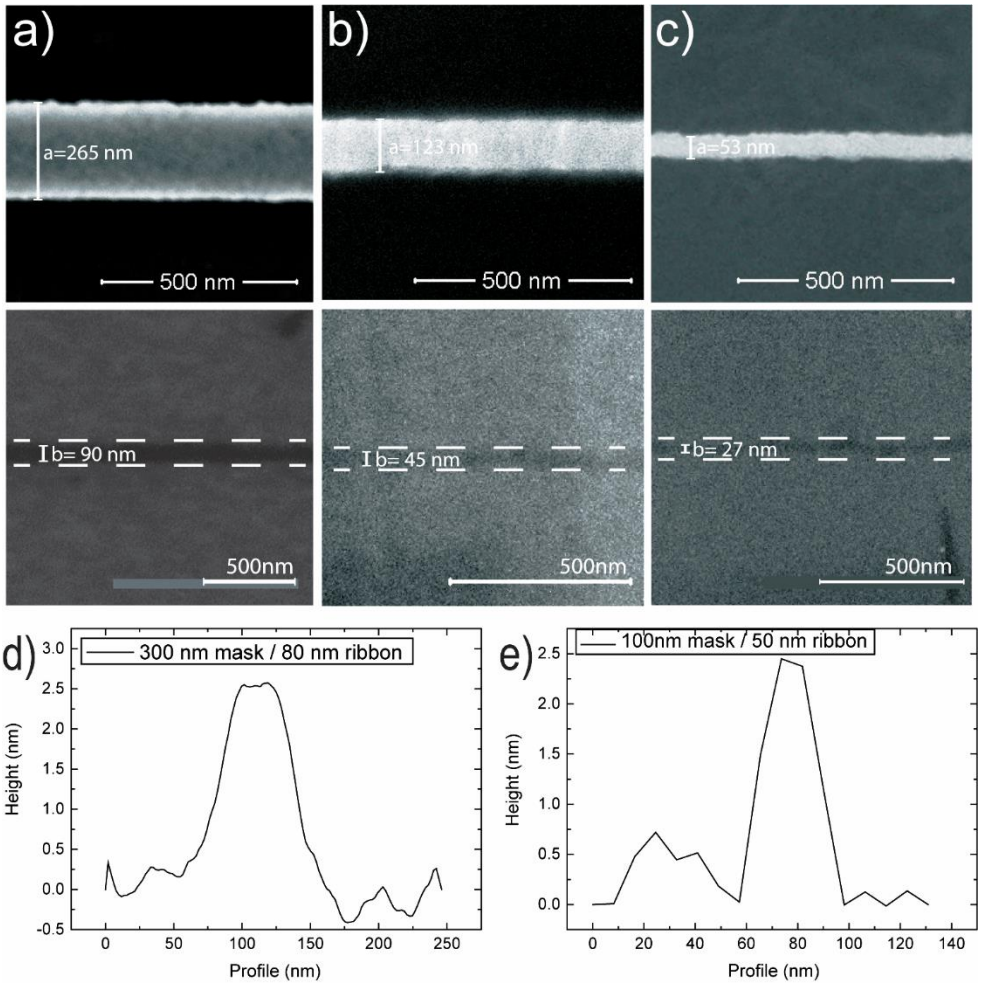

Figure III.2. Narrowing-down of graphene nanoribbons. From a) to c) SEM micrograph of metallic nanorods (top) of thicknesses respectively of 300 nm (aluminium), 100 nm (gold) and 50 nm (gold), and the graphene nanoribbons sculpted underneath in H_2 plasma (bottom). d) and e) AFM cross sections of graphene nanoribbons sculpted in H_2 plasma under metallic masks of respectively 300 nm aluminium and 100 nm gold.

III.V References

(1) Zhang, Z.; Du, J.; Zhang, D.; Sun, H.; Yin, L.; Ma, L.; Chen, J.; Ma, D.; Cheng, H.-M.; Ren, W. *Nat. Commun.* **2017**, *8*, 14560.

(2) Lee, J.-K.; Park, C.-S.; Kim, H. *RSC Adv.* **2014**, *4* (107), 62453–62456.

Appendix IV

Supporting Information to Chapter 6

IV.I Materials and Methods

IV.I.I Self-Assembled-Monolayer, SAM

A gold film was deposited on a Si/SiO_2 wafer (University wafer) via thermal resistance evaporation at $P < 1*10^{-6}$ mbar.

Next, a mixed self-assembled monolayer was formed on the gold film from a mixed solution of 1,11-amino undecanethiol (at) and 1-dodecanethiol (dt) in ethanol. Namely, a solution of 1,11-amino undecanethiol (at) 5mM in ethanol was mixed in a petri dish with a solution of 1-dodecanethiol (dt) 5mM in ethanol with volume ratios varying from 0 % to 100 %. The self-assembled monolayer formed by immersing the substrate into the petri-dish filled with the mixed solution of at and dt at room temperature, under argon atmosphere for approximatively 12 hours[1].

The at and dt solutions were prepared in bottom round flasks in ethanol and sonicated 10 minutes before being mixed in a petri-dish. All the wares were cleaned using a piranha solution (3:1 sulfuric acid and hydrogen peroxide). All the chemicals were purchased from Sigma-Aldrich®. The gold substrate was cleaned in O_2 plasma at 100 W, 0.5 mbar for 30 s (Diener plasma etcher).

The thickness of the SAM was determined by ellipsometry, Figure IV.1a. For ratios of at : dt above 40 : 60 the thickness of the SAM exceeded the thickness of a monolayer, in the order of 1 nm, indicating the formation of multilayers (disordered layers[1]). Next, the SAM formed from a mixed solution 30 : 70 = dt : at was characterized by X-ray photoelectron spectroscopy, Figure IV.1b. The NS1 and NS1a peaks respectively at 399 eV and 407 eV rise from the asymmetric bonds of N in the amine of the aminothiols that forms both N-C and N-H bonds, indicating the presence of aminothiols in the mixed SAM. The weak intensity of the N1S and N1Sa peaks is ascribed to the low content of nitrogen atoms in the SAM. In fact, each aminothiol contains one nitrogen atoms every eleven carbon atoms. Thus, statistically, one every ten molecules in each aminothiol contributes with a Nitrogen emission derived by a single nitrogen atom.

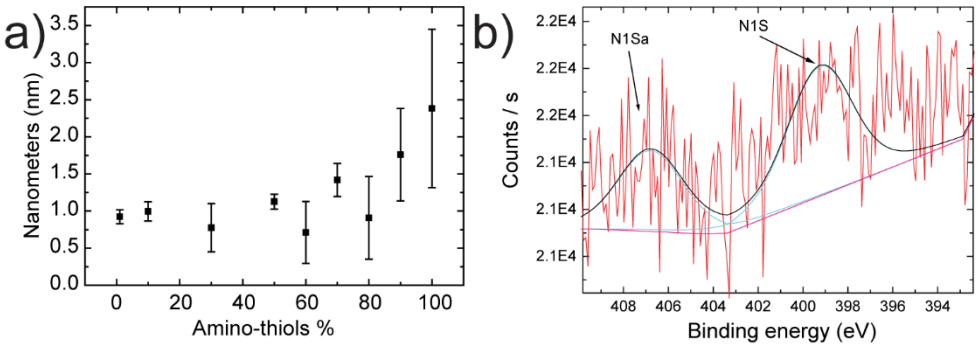

Figure IV.1. SAM characterization. a) Ellipsometry measurements of a SAM with various at/dt ratios. b) XPS analysis of the N1S and N1Sa peaks obtained from a SAM formed from a mixed solution of 30 : 70 = at : dt assembled on a gold substrate. The spectrum was acquired over 10 spots at a 0.01 eV excitation energy with an acquisition time of 9 s over a line sample of 400 µm using a K-Alpha XPS by Thermo Scientific (property of the technical university of Eindhoven).

IV.I.II Layer-by-Layer deposition

The multilayered film of polyelectrolytes was grown via Layer-by-Layer deposition, LbL, using poly (allylamine hydrochloride), PAH, (M_w = 17500 $gmol^{-1}$) and poly (sodium 4-styrenesulfonate), PSS, (M_w = 70000 $gmol^{-1}$) purchased from Sigma-Aldrich®. The film was grown on a Si/SiO_2 substrate coated with a gold film functionalized with a mixed SAM 30 : 70 = at : dt ratio.

To grow the multilayered film of polyelectrolytes, the substrate was alternatively dipped into a solution of PSS (3 mM in repetitive units) in 1:1 EtOH and 0.5 M NaCl in H_2O and a solution of PAH (3 mM in repetitive units) in 1:1 EtOH and 0.5 M NaCl in H_2O, at room temperature each time for 20 minutes. Between each layer, the substrate was rinsed with $EtOH/H_2O$ (1:1), and then dried under argon stream[2]. In order to promote the adhesion between the multilayered film of polyelectrolytes and the substrate, the first layer of PSS was deposited from an acidic solution of PSS in 0.5 M NaCl in 1:1 $EtOH/H_2O$, with H_2O previously adjusted at pH=2 by adding 40 µL of HCl (37% HCl in aqueous solution from Sigma-Aldrich) to 50 mL of ultra pure water. In fact, the acidic solution protonates the amines of the mixed SAM attracting the first, negatively charged PSS layer.

IV.I.III Microtomy of the metallic nanogaps

The gold layer comprising the multilayered film of polyelectrolytes was embedded within a photocurable polymer in order to be sectioned later via microtomy, forming nanogaps between metallic nanorods (where the gap spacing has the thickness of the LbL multilayer). First, a drop of photocurable polymer was casted over the gold/polyelectrolytes/gold stack on Si/SiO_2 and cured (see Appendix I.I.I). Next, the stack is lifted from the Si/SiO_2 substrate by intercalating a razor blade between the first gold layer and the SiO_2 substrate (see Figure 6.2a). Last, the stack is immersed into a PDMS mould filled with photocurable polymer and cured, yielding a polymer scaffold embedding the gold/polyelectrolytes/gold stack (see Figure 6.2b).

The transverse nanogaps were prepared by microtomy sectioning of the polymer scaffold embedding the gold/polyelectrolytes/gold stack. We employed a Leica® EM UC 6 microtome first trimming the polymer with a trimmer Diatome® trimtool 20®, then sectioning the polymer scaffold with an Ultra Diamond Knife 35®. The cutting proceeds with the blade parallel to the gold films (Figure 6.3 of Chapter 6), sectioning polymeric slabs 50 X 50 μm^2, 150 nm thick at a cutting speed of 1,6 mm/s.

IV.I.IV Thiolation of poly (allylamine hydrochloride) polyelectrolyte

A solution of 3,3'-dithiopropionic acid (DTPA) (55.9 mg, 0.266 mmol, 1.0eq), N-(3-dimethylaminopropyl)-N'-ethylcarbodiimide hydrochloride (EDC·HCl) (968.2 mg, 6.23 mmol, 23.4eq) and N-hydroxysyccinimide (NHS) (659.7 mg, 5.73 mmol, 21.5 eq.) in DMF (60 ml) was dissolved by sonication, Figure IV.2 a-i. The solution was stirred at room temperature under an argon atmosphere for 2.5 hrs and then evaporated via rotary evaporation[3]. The product was added to a solution of PAH (M_W 17500 $gmol^{-1}$; 99.4 mg, 5.68 µmol, 0.5 eq.) in H_2O/DMF (1 : 1, 40 mL), followed by the addition of dithioltheritol (DTT) (39mg, 0.256 mmol, 0.96 eq.), Figure IV.2 a-ii. The solution was stirred at room temperature under an argon atmosphere for 4 hrs and rotary evaporated. The product was added to a solution of 40 ml of trifluoroacetic acid (TFA) (1% in H_2O) with 2g of zinc and stirred at room temperature for 2 hrs, Figure IV.2 a-iii. Then, the solution was centrifugated for 10 min at 4000 rpm prior to dialysis using a 30kDa membrane. The dialysis was performed at room temperature to a total of 72hrs. The dialysis water was

replaced every 12hrs. The solvent was removed by rotary evaporation and freeze-dried.

Solid-state ^{13}C NMR of the resultant product, Figure IV.2b, shows two ill-resolved signals at 44.15 ppm and 36.78 ppm, which were assigned to the methylene moieties of the polymer backbone and attached thiopropionate, by comparison with unreacted PAH. Importantly, a signal at 172.98 ppm indicated the successful incorporation of the thiopropionate into the polymer. The solid-state ^{13}C NMR measurements were measured using a Bruker AV-I 750MHz spectrometer with 17.6 Tesla magnetic field. The ^{13}C were irradiated with 40.32 kHz radio frequency pulses with a contact time of 2 ms, and 10000 scans were acquired. All the ^{13}C spectra were externally referenced to methyl signal of TMS and were processed in Topspin 3.2 and MestReNova software.

To further prove the presence of thiol groups in the polymer, an Ellman's test was performed[4]. A sample of the product (0.5 mg) was dissolved in ultra pure water (3 mL) and diluted 1:100 into a solution of 0.1 M Na_3PO_4 and 1 mM ethylenediamine tetraacetic acid (EDTA). To the solution was then added 10 µL of Ellman's reagent, to generate 2-nitro-5-thiobenzoic acid (NTB). The concentration was determined using Beer-Lambert law, using an extinction coefficient of $\varepsilon = 14150\ M^{-1}cm^{-1}$. A total of 6.4 nmol was found.

All chemicals were purchased from Sigma-Aldrich and used without further purification.

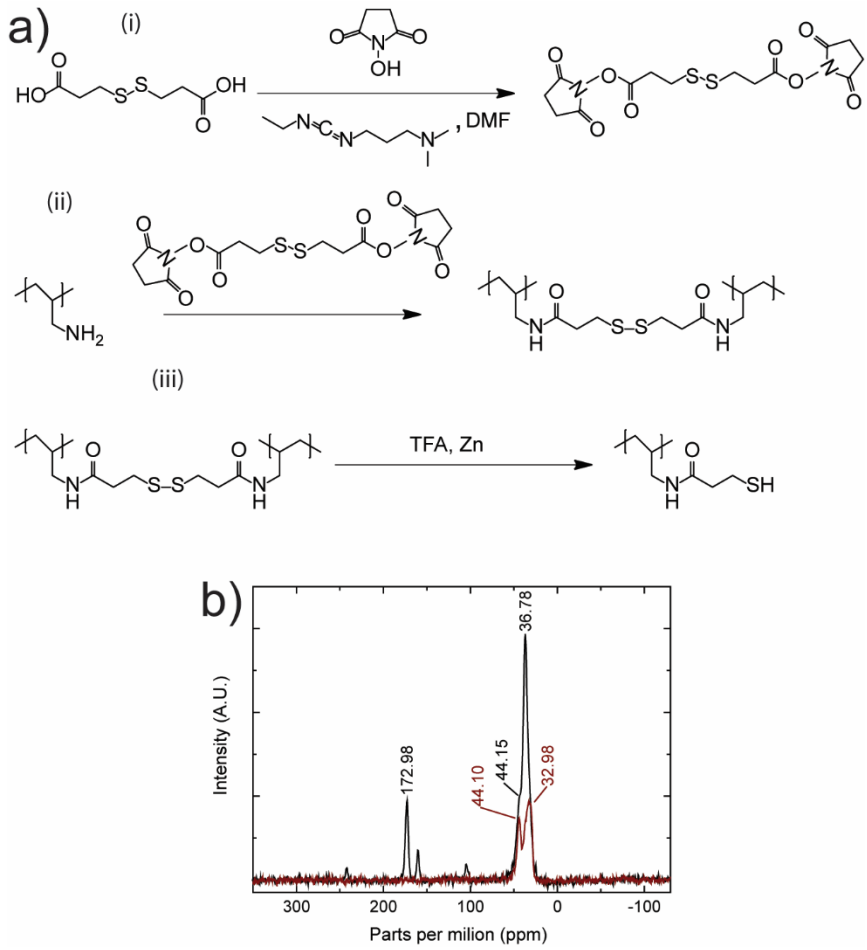

Figure IV.2. a) Thiolation of the PAH polyelectrolyte. b) ^{13}C solid state NMR of the pristine PAH (red curve) and the thiolated PAH (black curve). The peaks at 44.10 ppm and 32.98 ppm on the red curve were attributed to the methylene bridge respectively on the backbone of the pristine PAH polyelectrolyte and the amine. The peaks at 44.15 ppm and 36.76 ppm in the black curve result from the methylene bridges on the backbone of the polyelectrolyte and attached to the thiopropionate. The peaks at 110 ppm and 160 ppm represent contaminations.

IV.II References

(1) Graham, D.; Dingman, S. A Step-by-Step Guide for Solution Based Self-Assembly, Sigma-Aldrich https://www.sigmaaldrich.com/technical-documents/articles/material-matters/a-step-by-step-guide0.html.

(2) Lvov, Y.; Decher, G.; Sukhorukov, G. *Macromolecules* **1993**, *26* (20), 5396–5399.

(3) Sam, S.; Touahir, L.; Salvador Andresa, J.; Allongue, P.; Chazalviel, J.-N.; Gouget-Laemmel, A. C.; Henry de Villeneuve, C.; Moraillon, A.; Ozanam, F.; Gabouze, N.; Djebbar, S. *Langmuir* **2010**, *26* (2), 809–814.

(4) Ellman, G. L. *Arch. Biochem. Biophys.* **1958**, *74* (2), 443–450.

Appendix V

Supporting Information to Chapter 7

V.I Materials and methods

V.I.I Formation of the polymer matrix used for the embedding of the gold films

A gold film few tens of nanometres thick was deposited by resistance evaporation on top of a Si/SiO_2 wafer (purchased from University Wafers). Gold was thermally evaporated inside a high vacuum chamber at $P<10^{-6}$ mbar and its thickness monitored by a quartz crystal microbalance (Leiden University home built thermal resistance evaporator operating below $1x10^{-6}$ bar). After the evaporation, a polymeric mixture of pentaerythritol tetrakis (3-mercaptopropionate) (Sigma-Aldrich), PETMP, and 1,3,5-triallyl-1,3,5-triazine-2,4,6(1H,3H,5H)-trione (Sigma-Aldrich), TATAO, (with proven competence for microtomy process[1]) was drop-casted over the gold film. The mixture was stirred for 2 minutes and set to rest in the desiccator to remove any air bubble. Lastly, 1% in weight ratio of 2,2-dimethoxy-2-phenylacetophenone, DMPA, was added to the mixture as photo-initiator. The polymer was hardened in air under the irradiation of a 365 nm UV lamp for 30 minutes, 7000 $\mu W/cm^3$ at 38,2 cm of distance. After the curing, the gold with the polymer on top was carefully stripped-off from the Si wafer and re-embedded inside a PDMS mould filled with uncured polymer mixture and once again UV cured.

V.I.II Preparing the slabs

A gold film with a thickness of a few tens of nanometres was embedded inside a polymeric support and sectioned by ultramicrotomy[1]. The microtome was a Leica UC6 equipped with a DiATOME diamond trim of 20° for the sample preparation, and 45° for the sectioning of the polymer matrix into slabs, each including a gold nanorod. The thickness of the slabs ranges from 50 nm to 500 nm, finely tuned by motor-actuators of the microtome.

Upon cutting, the ultrathin slabs shifted towards the boat of the knife, which was filled with ultra pure water. The slabs floated on the boat exploiting the surface tension of the water. Then, a circular tungsten wire, around 0.5 mm radius (the perfect loop), was placed on the surface of the water surrounding the slabs. The surface tension between the wire and the water displaces a drop of liquid that

remains constrained inside the loop, enabling the transfer of the polymer slabs floating on surface of the trapped drop.

Subsequently, the perfect loop was positioned carefully close to the opening (d=30 μm to 50 μm) drilled in a glass substrate acting as the support for the slabs (NPC chips purchased from NanIon). The substrate was previously oxidized inside an environmental plasma at 7×10^{-2} mbar for 15 s, promoting the hydrophilicity of the glass. While the surface of the glass was still wet, we used a microstep manipulator (Thor-Labs) to gently move the slabs over the glass substrate in order to align the gold nanorod across the glass opening.

The position of the slab was adjusted during the slow evaporation of the water in order to maintain in place the gold nanorod across the window of the membrane. Additionally, the plasma oxidation of the membrane allowed the uniform evaporation of the water from the surface, avoiding the misalignment of the slabs induced by sudden water displacements. Finally, the water completely evaporated and the slab fully adhered on the surface of the membrane.

Subsequently, the membrane was placed inside a 40°C oven to completely evaporate the water residuals trapped between the surface and the polymer slab. Afterwards, the protocol was accurately repeated in order to deposit a second slab. The orientation of the slabs was in a way that the embedded gold nanorods form a misalignment angle of ~90°.

Further then, both sides of the membrane were exposed to a 0.5 M solution of KCN in ultra pure water, which etches the gold nanorods and forms a nanopore. The sample was then rinsed three times in ultra pure water to remove any etchant residuals and, then, dried under vacuum.

V.I.III Nanopore experiments

Samples prepared with the precise alignment of the slabs, after etching away the gold lines, were mounted in a custom-made flow cell out of PEEK (Figure V.1). The design of the flow cell provides sufficient sealing on either side of the glass support. The measurements were performed by injecting buffer solutions (both KCl and LiCl) with different concentrations ranging from 1 mM to 1 M containing 10 mM Tris-HCl and 1 mM EDTA. To drive the electrophoretic flow of ions, transmembrane

potentials were applied to Ag/AgCl electrodes, pre-mounted on the flow cell. A resistive feedback amplifier (Axopatch 200B, Axon Instruments) and digitized at 500 kHz measured the corresponding current traces.

For translocation detection experiments, 48.5 kbp unmethylated λ-DNA (10 ng/ µL, reference no. D152A, lot no. 27420803, Promega, Madison, WI) was used. The event detection and sorting were performed by the Matlab based Transalyzer package[2].

V.I.IV The nanopore set-up

Ionic conduction was measured in a custom-design flow-cell made out of PEEK. Figure V.1a and V.1b illustrate the design: two main reservoirs (cis and trans) were linked through a nanopore deposited on a glass support, namely an NPC-Chip (Nanion Technologies, NPC®-Chips). Each chamber was equipped of three inlets, two for the flow of the ionic solution and one for the electrodes.

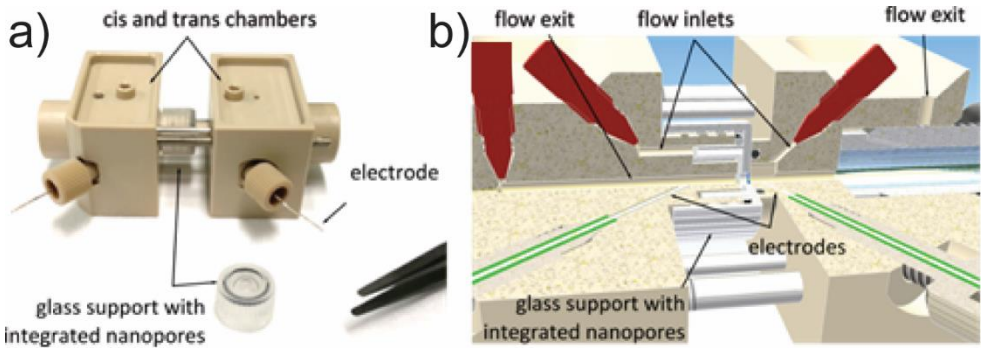

Figure V.1. Experimental set up. Optical micrograph (a) and schematics (b) of the home-made experimental setup: different components are marked on the images.

V.II Access resistance of a rectangular area: theoretical model

An interfacial nanopore is defined by two crossing nano-slits that are carved through their respective nano-membranes stacked together. The top-view of the nanopore usually assumes a parallelogram with its angles determined by the membrane stacking and its side lengths determined jointly by the membrane stacking as well as by the original widths of the slits. Two different types of access resistances prevail for ions that will eventually pass through the nanopore. The ions diffuse from the bulk electrolyte to the slit on the *cis* side as well as from the

slit to the bulk electrolyte on the *trans* side. They are subsequently pulled into/out the nano-trenches (defined by sealing one side of the nano-slides by the other membrane) by the electric field. The sum of those resistances accounts for the trench access resistance $R_{a,t}$. Then, the ions in the trenches diffuse and drift to the nanopore and finally pass through. This process generates another access resistance named pore access resistance $R_{a,p}$. The path of the ions is symmetric on both sides of the pore. Thus, the total pore resistance, R_t, is (1):

$$R_t = 2R_{a,t} + 2R_{a,p} \qquad (1)$$

In order to calculate the access resistance, we first calculate the corresponding capacitance, *C*, for an equivalent electrode with the same shape of the access area. It is a rectangular strip for $R_{a,t}$ and a parallelogram for $R_{a,p}$. The resistance can then be derived via[3] (2):

$$R = \frac{\varepsilon_0 \rho}{C} \qquad (2)$$

where, ε_0 is the permittivity of vacuum and ρ is the resistivity of the electrolyte. The electric field lines in the capacitor are analogues to the current lines in the resistor.

For *C* corresponding to $R_{a,t}$, the opposite electrode has an infinite area placed infinitely away from the equivalent electrode with the rectangular strip trench area (see above). For *C* corresponding to $R_{a,p}$, the opposite electrode has an area equal to that above the pore with a distance equal to the slab thickness, *h*. The rectangle and parallelogram electrodes are assumed to carry positive charge with a uniform charge density. The electric field strength along the central axis can be obtained by integrating the charge on the electrodes. By integrating the electric field strength along the central axis, the electric potential is found. This leads to the calculation of *C* as the following (3):

$$C = \frac{Q}{\Delta U} = \frac{\sigma A}{\Delta U} \qquad (3)$$

where, *Q* is the total charge on the electrode, ΔU is the potential drop between two electrodes, σ is the charge density, and *A* is the area of the

rectangular/parallelogram electrode. Equation (2) should be multiplied with a factor of 2 when calculating *R* in order to count for the fact that *C* is calculated for the whole space while the ions only enter the pore from one side of the membrane stack.

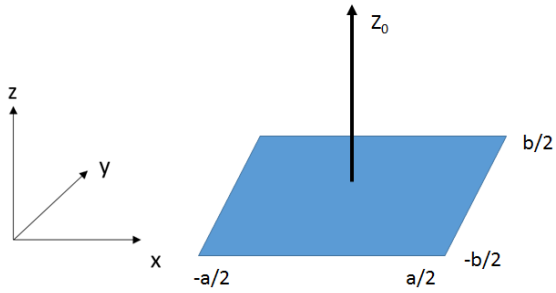

Figure V.2. Geometry of interfacial nanopore, used for simulation.

If the two slits are placed orthogonal to each other so that the top-view of the pore is a rectangle, an analytical solution to *R* exists. As illustrated in Figure V.2, the electrode carries charge with a uniform density, *σ*. The width of electrode is *a* and length is *b*. The electric field strength at height *z* along the central axis can be obtained by (4):

$$E(Z)=\frac{\sigma}{4\pi\varepsilon_0}\iint_{area}\frac{dxdy}{x^2+y^2+z^2}\frac{z}{\sqrt{x^2+y^2+z^2}}=\frac{\sigma z}{4\pi\varepsilon_0}\int_{-a/2}^{a/2}\int_{-b/2}^{b/2}\frac{dxdy}{(x^2+y^2+z^2)^{3/2}}$$

$$=\frac{\sigma z}{4\pi\varepsilon_0}\int_{-b/2}^{b/2}\frac{ady}{\sqrt{a^2+y^2+z^2}(y^2+z^2)} \quad (4)$$

Equivalent to (5):

$$E(z)=\frac{\sigma}{4\pi\varepsilon_0}arctan\left(\frac{ay}{z\sqrt{a^2+z^2+y^2}}\right)\Big|_{b/2}^{-b/2}=\frac{\sigma}{4\pi\varepsilon_0}arctan\frac{ab}{z\sqrt{a^2+z^2+b^2}} \quad (5)$$

By integrating the electric filed strength along the *z* direction, we can get the potential as follows (6):

$$U(z_0) = \int_0^{z_0} E(z)dz \quad (6)$$

Equivalent to (7):

$$U(z_0) = \frac{\sigma}{4\pi\varepsilon_0}\left(z_0 \arctan\frac{ab}{z_0\sqrt{a^2+b^2+z_0^2}} - a\arctan h\frac{\sqrt{a^2+b^2+z_0^2}}{b} - b\arctan h\frac{\sqrt{a^2+b^2+z_0^2}}{a}\right)$$

$$= \frac{\sigma}{4\pi\varepsilon_0} L(a,b,z_0)$$

(7)

i.e. L(a,b,z$_0$) is introduced to denote the calculation in the parentheses. Hence, the capacitance, *C*, of this rectangular electrode with an opposite electrode with an equal potential surface placed at distance *s* is (8):

$$C = \frac{Q}{U} = \frac{ab\sigma}{U(s) - U(10^{-10})} = \frac{4\pi\varepsilon_0 ab}{L(a,b,s) - L(a,b,10^{-10})} = \frac{4\pi\varepsilon_0 ab}{F(a,b,s)} \quad (8)$$

Since the potential at zero distance from the electrode is infinite, the potential at 1 Å is assigned as the reference and *F(a,b,s)=L(a,b,s)-L(a,b,10^{-10})* is introduced. If *s* tends to infinity, *C* asymptotically approaches a constant value; it is the capacitance of two rectangular electrodes separated by an infinite distance. Finally, the access resistance, R_a, is (9):

$$R_a = \frac{2\varepsilon_0\rho}{C} = \frac{\rho}{2\pi ab}F(a,b,s) \quad (9)$$

However, for pores with a general parallelogram-shape, the integration of electric field strength can be done only in a numerical way. In what follows, modelling results are shown for a pore formed with two identical membranes of thickness *h* and slit (trench) width *a*. The angle between the crossing slits is ϑ. The slit/trench length *L* = 1 mm is very large compared with *a*. For a 1 M KCl solution, ρ = 0.1 Ω·m. The modelling results are summarized in the table below.

a (nm)	*h* (nm)	ϑ (°)	$R_{a,t}$ (Ω)	$R_{a,p}$ (kΩ)
20	100	90	382	2,620
20	10	90	382	1,518

200	100	90	310	154
200	100	30	310	82

Obviously, For the dimensions typical in this work, $R_{a,p}$ is fund to be larger than $R_{a,t}$ by at least two orders of magnitude. Therefore, $R_{a,t}$ can be neglected.

This model is approximate because *C* is calculated in free space around the pore area, a simplification of the situation with the ion paths being confined by the sidewalls of the trenches on both sides of the membrane stack. This model does not consider possible contributions of surface conductivity from the electrical double layer on the pore surface, which may influence the linear relationship between conductance and salt concentration. To compensate for such deficiencies, two coefficients *γ* and *n* are introduced as fitting parameters in R_t (10):

$$R_t = 2\gamma \frac{2\varepsilon_0 \rho \Delta U}{\sigma A} = \gamma \frac{F(a,b,h)}{\pi abqc^n(\mu_+ + \mu_-)} \quad (10)$$

where, *a* and *b* are the side lengths of the pore area, *c* is the salt concentration in the electrolyte, *q* is elementary charge ($1.6 \cdot 10^{-19}$ C), μ_+ and μ_- are mobility of cation and anion, respectively, *h* is the thickness of membrane (i.e. depth of the trenches) and *F* is a function of *a*, *b* and *h* as described in Supporting Information.

V.III COMSOL simulation

We simulated the ionic current of the interfacial nanopore using COMSOL Multiphysics. The motion of ions in electrolyte is described by the Nernst-Planck equation (NPE), while the electric potential distribution is described by the Poisson equation (PE). In simulation, the "transport of diluted species" module (NPE) and the "electrostatics" module (PE) were fully coupled to govern the system of a three-dimension model. For KCl solution, the mobility of K^+ and Cl^- are 6.95×10^{-8} m^2/Vs and 7.23×10^{-8} m^2/Vs, respectively[4]. The diffusion coefficients were determined by referring to the Einstein relationship. All the interfaces in the system were neutral and the voltage bias was set at 0.2 V. The total current was a numerical integration of the ion flux density in the pore area. Figure V.3 shows the distribution of current density and electrical potential in nanopore structure from the COMSOL simulation.

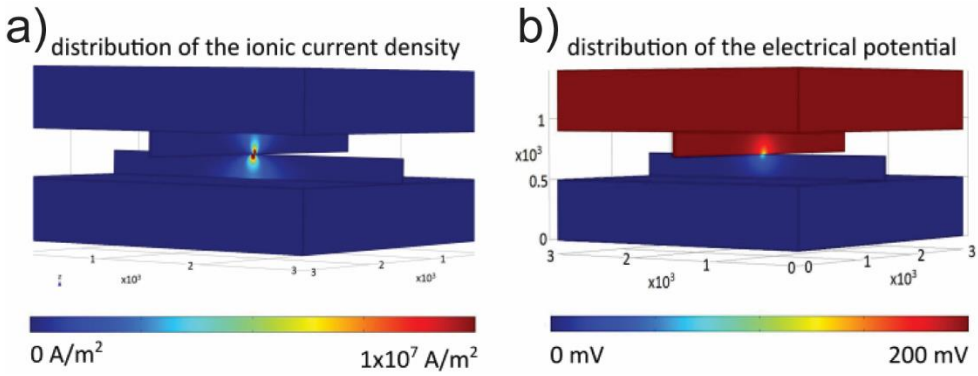

Figure V.3. COMSOL simulation of the ionic current density (a) and electrical potential (b) distribution of an interfacial nanopore with h = 200 nm and a = 10 nm. The simulations consider buffer solution of 1 M KCl and under the applied transmembrane potential of 200 nm.

V.IV Detection of translocated DNA by PCR

To verify that Lambda DNA was translocated to the trans chamber during the experiment, we used polymerase chain reaction (PCR). PCR is a very sensitive assay that is capable of detecting minute amounts of DNA. We chose to amplify a region of 449 bp corresponding to nts 24201-24649 of lambda DNA (48502 bp) using the forward primer Lamfor (5'-ggtgaacttccgatagtgcggg-3') and reverse primer Lamrev (5'-gcaacgtttcagcagctacagtcag-3'). Conditions for PCR were as follows: total volume 12.5 µl, 1 unit of Pfu Polymerase (Thermo Fischer Scientific), Pfu buffer plus $MgSO_4$, primers 200 nM, dNTPs 200 µM , 0.5 µl chamber sample. Program: 3 min 94 ºC, 35 cycli of 1 min 94 ºC, 1 min 57 ºC , 1 min 72 ºC.

PCR products were electrophoresed on a 1.5% (w/v) agarose gel in TAE buffer (40 mM Tris, 20 mM acetic acid, and 1 mM EDTA). Inset Figure 7.3a (Chapter 7) shows the result of PCR after 35 cycles. Lane 2 showed that before the translocation reaction no Lambda DNA could be detected in the bottom compartment (the band that is visible corresponds to the input primers that migrate near the 100 bp DNA fragment from the DNA ladder (lane 1). Lane 3 showed that after translocation, a PCR fragment of the correct size could be obtained. This product had the same size as that of lane 4 which was obtained by PCR using 3 pg of pure lambda DNA (i.e. the positive control). In lane 5 instead of lambda DNA, water was added to the PCR

(negative control). From these data we could conclude that lambda DNA was indeed translocated to the trans chamber.

V.V Characterization of DNA translocation

We probed the translocation of the dsDNA through the same interfacial nanopore shown in Figure 7.4a of the main text by varying the transmembrane potential and the LiCl buffer concentration. The data are plotted in Figure V.4. Note that the data in blue and green colours corresponded to the populations shown in Figure 7.4b (Chapter 7) with the same colour.

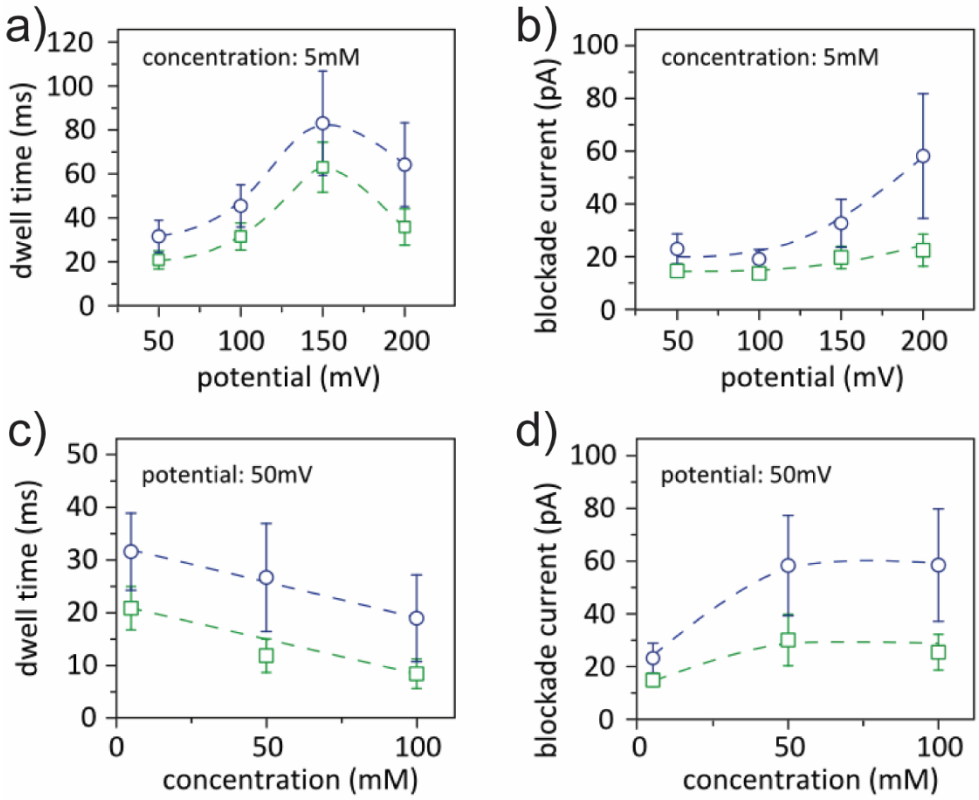

Figure V.4. Characterization of the DNA translocation through an interfacial nanopore. a) and b) translocation with different potentials. c) and d) translocation at different LiCl concentrations. The data in blue and green colours correspond to the evolution of the two major populations of the data shown with the same colours in the Figure 7.4b (Chapter 7).

The dwell time in conventional nanopore systems is largely dependent on the applied transmembrane potential (for a constant ionic strength). Lowering the potential weakens the electrostatic force acting on the DNA molecule and reduces the translocation speed (i.e. increases the dwell time). One could observe this behaviour in our system upon lowering the potential from 200 mV to 150 mV (Figure V.4a). The dwell time of the DNA, however, decreased at < 150 mV. With the low transmembrane potential and ionic strength used in our measurement, effects related to surface charges[5] and DNA/nanopore interaction played complex roles. Understanding the interplay between those forces within our novel architecture involving polymeric materials (rarely used and studied compared to solid state materials) invoked substantial further theoretical and experimental investigations.

Varying the concentration of the DNA in the buffer solution provided more insights into the translocation mechanism. We studied DNA translocation at two concentrations, 10 ng/µl and 20 ng/µl (Figure 7.3b Chapter 7 and Figure V.**5**) through the same nanopore. Doubling the DNA concentration only slightly increased the capture rate − the rate at which DNA molecules were captured by and subsequently translocated through the nanopore − from 400 up to 430 events in 10 minutes of experiment. Obviously, the capture rate in interfacial nanopores failed to scale proportionally with DNA concentration, unlike what has been reported for conventional nanopores[6]; This observation could imply the presence of a strong drag force, e.g. the DNA/nanopore interaction with a more dominant role than the accessibility of the DNA for the translocation. This conclusion was further backed-up by considering that our measured capture rates were few orders of magnitudes lower than those reported for conventional nanopores[7-9].

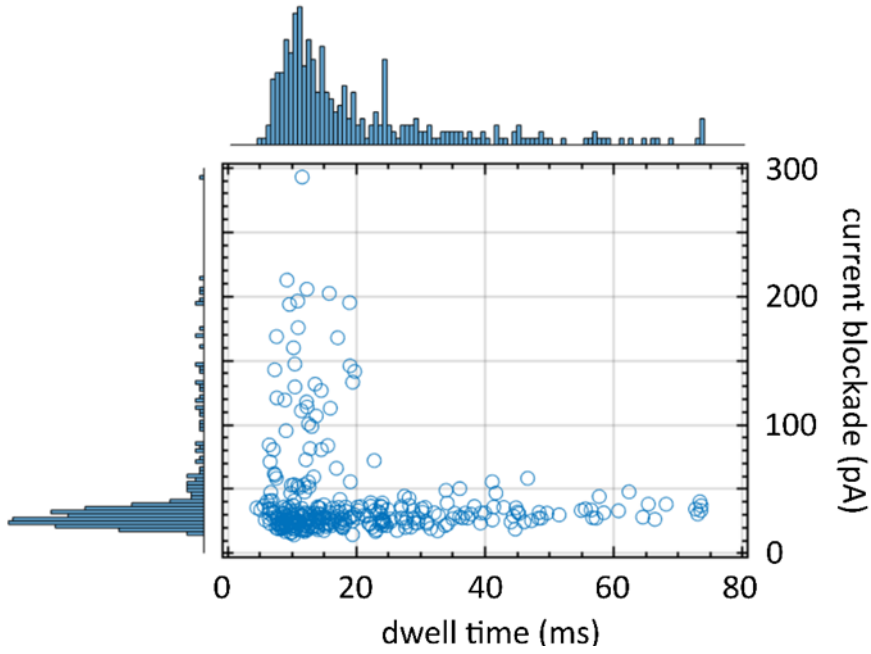

Figure V.5. Scatter plot of the amplitude of the current blockade versus translocation time for DNA translocation events through the same nanopore as in Figure 7.4a of Chapter 7. The measurement was performed under the same conditions as in Figure 7.4a except that the DNA concentration was doubled (to 20 ng/µl). The plot features ~430 translocation events, recorded during 10 min of experiments. The distributions of the dwell time and current blockade were separately plotted in left and top inset panels.

V.VI Simulation of the DNA translocation in an interfacial nanopore

Figure V.6 shows the ionic waveform of translocation event simulated by COMSOL. Parameters a and h were both set at 50 nm and the radius of DNA is set at 5 nm. Using the actual radius of dsDNA (r = 1 nm) gave rise to a very high mesh density with unacceptable simulation time. So, we used r = 5 nm instead for illustration. This modification might have only influenced the blockage level (the change of current) and would have not impacted the shape of the waveform. We used the salt concentration and the bias voltage of 100 mM and 200 mV, respectively. Since the position of DNA was manually set step by step, the translocation speed was not affected by the bias voltage. Any possible DNA-nanopore interaction was omitted in this modelling attempt. The simulation returned with a sharp

translocation waveform both at the start and the end of the event, in the absence of any interaction between DNA and interfacial nanopores.

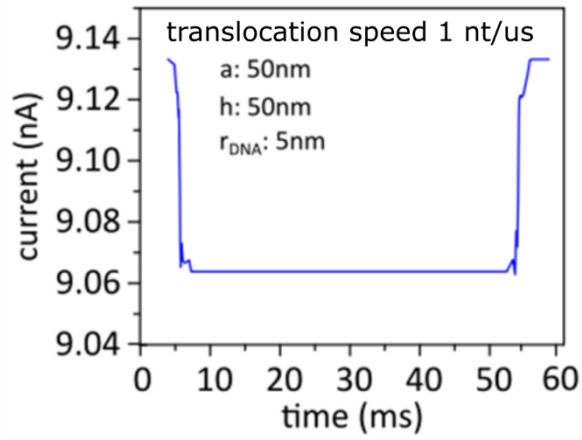

Figure V.6. COMSOL simulation result of a DNA translocation through an interfacial nanopores with the same geometry as in Figure 7.4a of Chapter 7.

V.VII Effective thickness of nanopore

The electrical resistance of a nanopore intuitively was dominated by that of the most restrictive region, i.e. the pore itself where the electric field was the strongest. Thus, the effective thickness of nanopore could be defined by referring to the profile of the electric field along the central axis perpendicular to the nanopore area. Specifically, the effective thickness was twice the distance from the pore centre to the point where the electric field intensity dropped to e^{-1} of its peak value for the symmetric system we were considering with regard to geometry and properties of membrane material and electrolytes.

We simulated the electric field distribution of interfacial and conventional nanopores of varied thicknesses using the COMSOL Multiphysics software package (Figure V.7a to V.7d). The centre of the nanopore was set at the origin of the coordinate system. The membrane thickness of the conventional nanopore was 2*h*, in order to compare with its counterpart interfacial nanopore that was formed by stacking two membranes, each with thickness *h*. The two slits of the interfacial nanopores were assumed to be perpendicular to each other. The conventional nanopore was further assumed to take a square shape instead of the commonly encountered circular one. With the definition above, the effective thickness of the

ordinary nanopore could be approximately viewed as the sum of its membrane thickness ($2h$) and twice the thickness of the access region commensurate with half the side length of the pore, a.

Although the interfacial nanopore exhibited obvious advantages (measured by effective nanopore thickness) over conventional nanopore for large h as seen in Figure V.7e and Figure 7.5 (Chapter 7), it was of general interest to minimize h for sequencing purposes. Figure V.7f separately compares the thicknesses of access and pore regions of conventional nanopores with the effective thickness of interfacial nanopores for very thin ($h \leq 5$ nm) nanopores. Obviously, in this regime the effective thickness of interfacial nanopores converged towards that of the access region of the conventional nanopores. Here, interfacial nanopores were clearly advantageous since they had no pore region. Indeed, the zero pore thickness of interfacial nanopores was always smaller than the finite pore thickness in conventional nanopores. However, the benefit of interfacial nanopores could only be fully exercised if the effective thickness of the access region was reduced e.g. by lowering a.

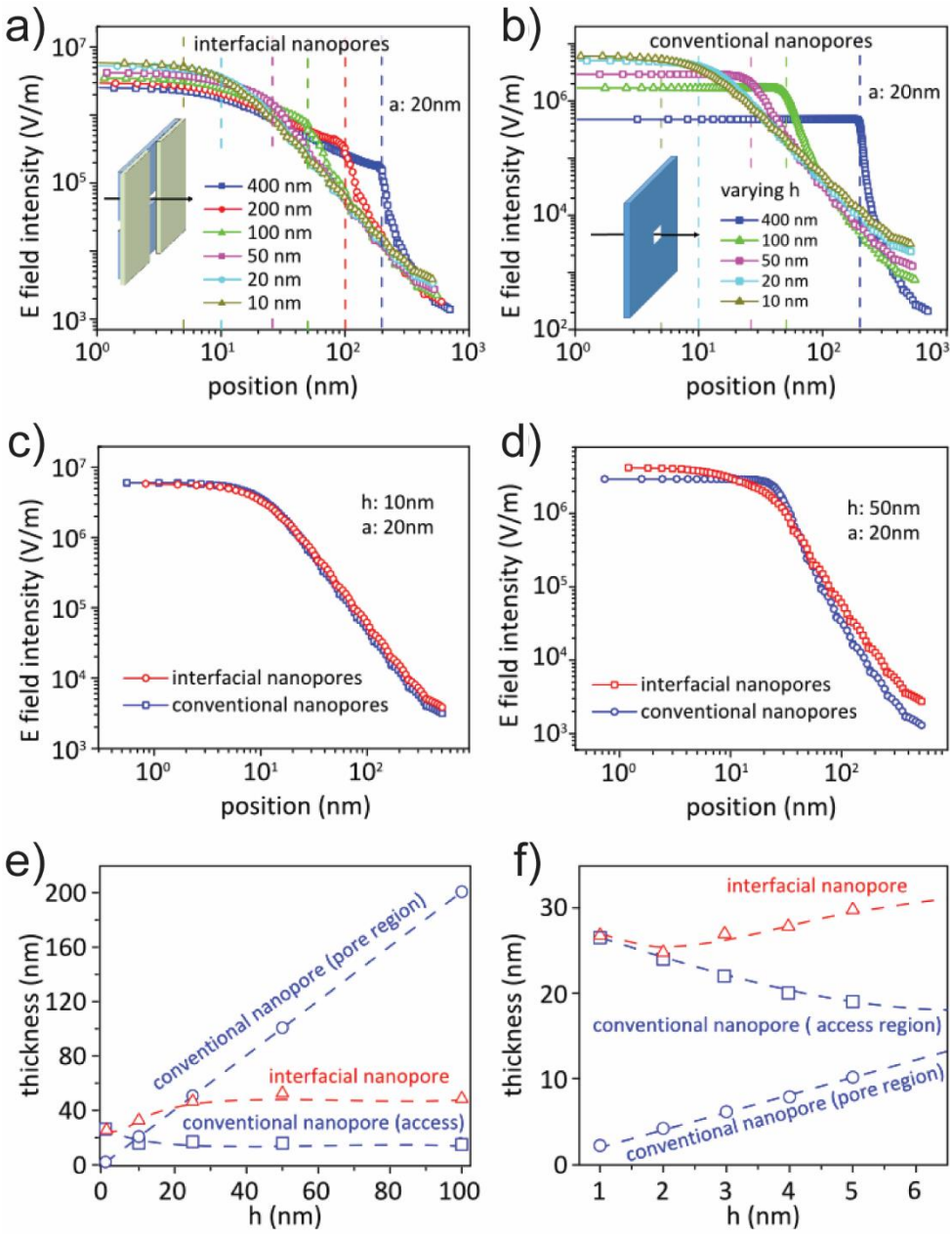

Figure V.7. Gradient of the electrical field profile near the conventional and interfacial nanopores. a and b) Electric field profiles for (a) interfacial and (b) conventional nanopores with different membrane thickness *h* but fixed pore size *a* = 20 nm. Conventional nanopores of squared shapes were considered to match the geometry of interfacial nanopores. c) and d) Comparison of the electric field profiles of conventional (blue lines)

and interfacial (red lines) nanopores with *a* = 20 nm for (c) *h* = 10 nm, and (d) *h* = 50 nm. e) and f) Simulation of the characteristic thicknesses of conventional (two-component) and interfacial (single-component) nanopores, plotted in different ranges.

V.VIII Sensitivity of interfacial nanopores

Resolution and sensitivity are the parameters quantifying the ability of a nanopore to resolve an analyte. Resolution represents the capability of the nanopore in resolving short (in length) objects and patterns present in the analyte (e.g. nucleotides on a DNA strand) and depends on the length of the narrowest area of restriction in the flow of ions (normally equivalent to the thickness of the membrane in conventional nanopores)[10]. In the main text, we mathematically illustrated that the resolution of interfacial nanopores − having zero physical length, even shorter than the monoatomic thickness of 2D nanopores − outperforms all existing nanopores.

Sensitivity, on the other hand, defines the capability of the nanopore in detecting small changes in the outer diameter of the analyte and depends on how tightly the nanopore "hugs" the translocating molecule[10]. Here, the sensitivity could be roughly expressed as the arithmetic sum of two components one from the pore region and one from the access region (11):

$$S = R_{pore}\left(\frac{v_{pore}}{V_{pore}}\right) + R_{acc}\left(\frac{v_{mouth}}{V_{mouth}}\right) \quad (11)$$

Here, R_{pore} was the pore resistance, R_{acc} was the access resistance, V_{pore} was the volume of the pore, V_{mouth} was the volume of the mouth of the pore (corresponding to the access resistance), v_{pore} was the volume of the external molecule inside the pore and v_{mouth} was the volume of the external molecule inside the mouth of the pore. Note that except for ultra-thin membranes, a DNA nucleotide (or small DNA gyration) that was enclosed entirely inside the pore region of a conventional nanopore did not occupy any volume corresponding to the access resistance. Hence, the first term was dominant for conventional nanopores while the second term (in the absence of any pore volume) was relevant for interfacial nanopores. Furthermore, as illustrated in Figure 7.2 (Chapter 7), the resistance of interfacial nanopores approached many of the other conventional nanopore systems; hence we excluded R_{pore} and R_{acc} in our discussions below.

We considered two nanopore systems: i) an interfacial nanopore of slab thicknesses *h* and trench width *a* and ii) a square shape conventional nanopore of lateral size *a* and total thickness 2*h*. The parameters were illustrated in the schematics of Figure V.8. V_{mouth} in the conventional nanopore system could be approximated by a hemisphere of radius *r* (*r* = *a*/2) on each side of the membrane; the hemisphere approximation became better for circular nanopores. Similarly, V_{mouth} in the interfacial nanopore scaled with *a*/2 (*a*: width of the trench) and was independent of *h* (inset in Figure V**.8**b). In contrast, the pore volume in the conventional nanopore scaled with *h* (inset in Figure V**.8**a). Hence, the comparison of the sensitivity of interfacial and conventional nanopores corresponded to the comparison of parameters *h* and *a*.

Accordingly, keeping the trench size (*a*) smaller than the total thickness of the membrane (2*h*) was an important consideration in order to maximize the sensitivity of interfacial nanopores. Note that for ultrathin membranes (*h* is comparable to the size of a nucleotide e.g. in graphene nanopores), both the volume of the pore and that of the pore mouth were in play in conventional nanopores; hence the sensitivity of interfacial nanopores was slightly superior, even for large *a*.

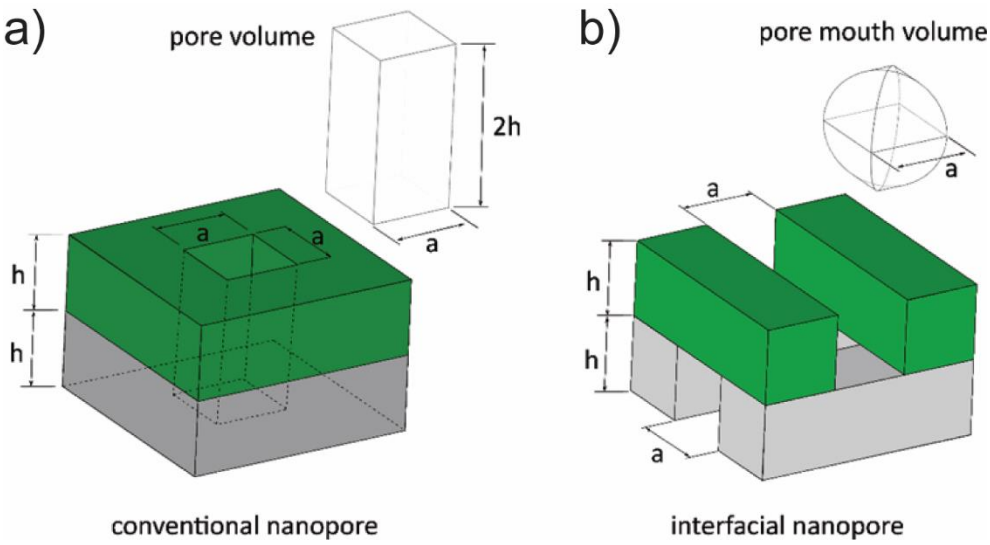

Figure V.8. Schematic representation of the geometry of (a) conventional and (b) interfacial nanopores used for our simulations.

Similarly to the study reported in ref [9], we have simulated and compared the distribution of the electric field in interfacial and conventional nanopore systems of Figure V**.8** for two different regimes: i) $h \geq a$ and ii) $a > h$.

For $h \geq a$ (Figure V.9a, and V.9b), the electric field of interfacial nanopore (b) was concentrated around the pore opening. The high-field region (*i.e.* the effective thickness) was much shorter than that in conventional pore (a) with the same size and membrane thickness. When $a > h$ (Figure V.9c and V.9d), the interfacial nanopore (d) exhibited a similar electric field distribution as in the conventional nanopore (c), which indicated a similar sensitivity. Note that the electric field distribution governed the "effective thickness" of a nanopore (the distance over which the field fell to 1/e of its maximum value).

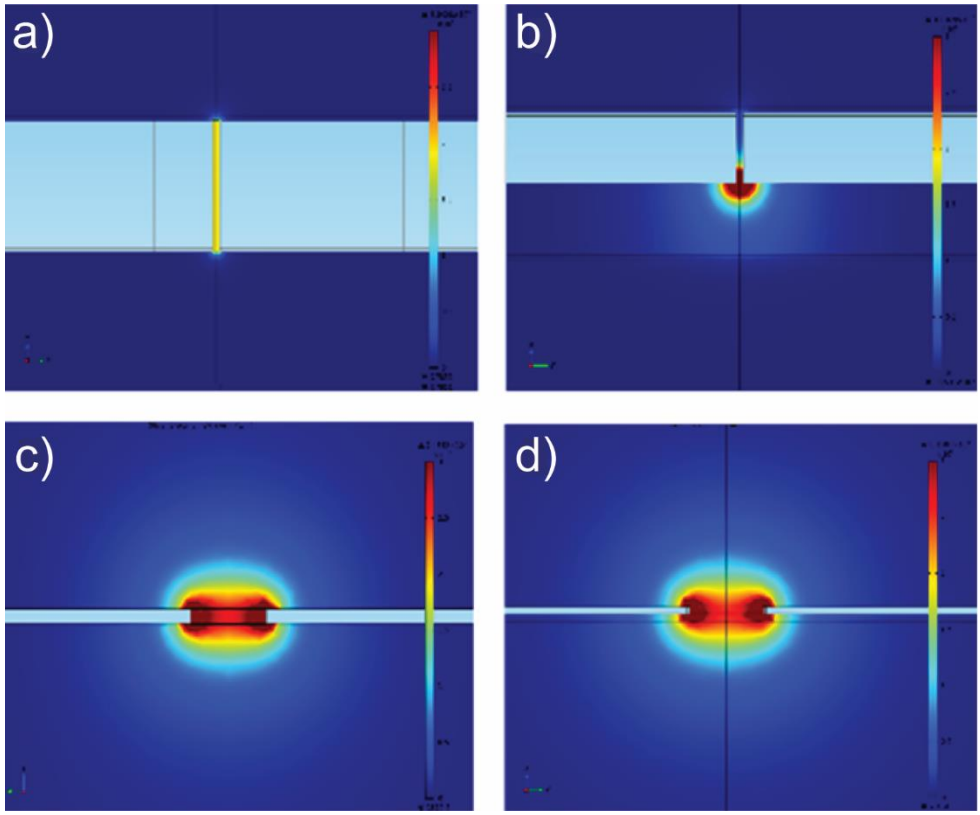

Figure V.9. Distribution of the electric field in different nanopore systems. a) Conventional nanopore with a = 5 nm and 2h = 100 nm. b) Interfacial nanopore with a = 5 nm and h = 50 nm. c) Conventional nanopore with a = 50 nm and 2h = 10 nm. d) Interfacial nanopore with

a = 50 nm and *h* = 5 nm. The simulation was done with 1 M KCl under 0.2 V bias voltage and the panels show the side view representations. The colour bar range is 0 to 3×10^6 V/m.

As a complementary study, we also simulated the waveform associated with the translocation of a nanoparticle through conventional and interfacial nanopores of *a* = 50 nm, *h* = 50 nm in Figure V.10. The radius of the nanoparticles was set as 5 nm which approaches the gyration radius of a short DNA/RNA strand and some large proteins.

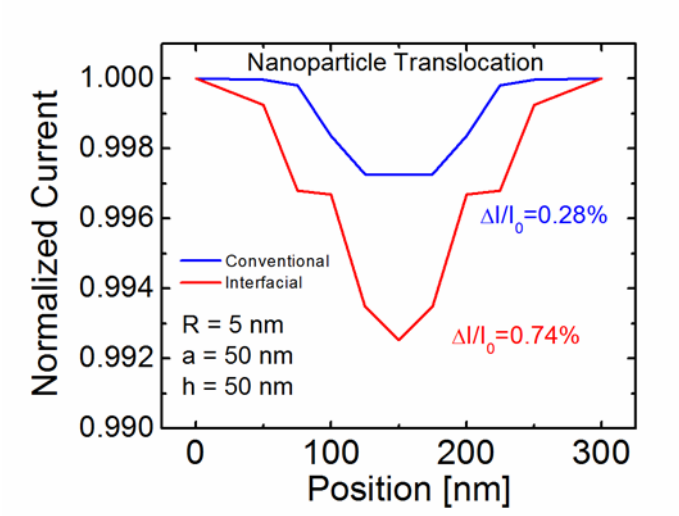

Figure V.10. Translocation waveform of a nanoparticle through conventional and interfacial nanopores. The current was normalised to its open pore state current.

The amplitude of the signal in the interfacial nanopore was significantly larger than that of the conventional nanopore which is due to the smaller volume of the mouth of the nanopore with respect to the total volume of the pore. Indeed, the electric field in the interfacial nanopore was confined in a smaller space compared with the conventional one with the same size, hence the translocation waveform showed a sharper peak when the particle passes through the nanopore centre, where the electric field reached its maximum value.

V.IX Noise analysis

Interfacial nanopores showed the characteristic $^1/_{f^2}$ noise. To the best of our knowledge, only two studies have reported $^1/_{f^2}$ noise in conventional nanopores [11,12] which may help to elucidate the background phenomenon in our nanopores as well. In nanopores drilled in some polymeric materials, the momentary opening-closing the channel by cleaved polymer strands (dangling ends) present at the pore rim was postulated as the origin of $^1/_f$ noise [11]. In the time domain, such noise was characterized by sudden transitions of the conductance between multiple (usually two) levels. The fluctuations were missing in nanopores in polymers with more stable subunits constituting the channel walls, leading to the $^1/_{f^2}$ noise dependency. As the interfacial nanopores exhibited the same characteristics both at time and frequency domains (at typically used transmembrane potentials) we considered the absence of the dangling ends as the origin of the observations. Indeed, in the interfacial nanopores the area close to the pore were fabricated upon moulding (curing) the polymer; hence, in contrast to the techniques based on drilling (breaking) the membrane, no dangling ends were anticipated. The presence of the nanosized air bubbles in the buffer solution also was capable of distorting the noise characteristics of a nanopore towards $^1/_{f^2}$ [12]. Such bubbles might be even large enough to trigger solitary jumps (as oppose to multiple transitions observed in the $^1/_f$ noise) in the conductance upon passage through the pore area. We have observed similar jumps in the conductance of some of the samples; hence the presence of nanobubbles in nanopore might have been also postulated as the origin of the observed $^1/_{f^2}$ behavior in interfacial nanopores. Indeed, the trapped air in between the two polymeric slabs upon fabrication could serve as a continuous source of injecting such bubbles. On the basis of the discussion here, a systematic study was demanded to understand the observed $^1/_{f^2}$ noise in the interfacial nanopores. We noted that, at first glance, no direct link between either of the discussed scenarios and the observed turn-over between the $^1/_{f^2}$ to $^1/_f$ noise upon increasing the transmembrane potential (Figure V.11a and V.11b) could be considered.

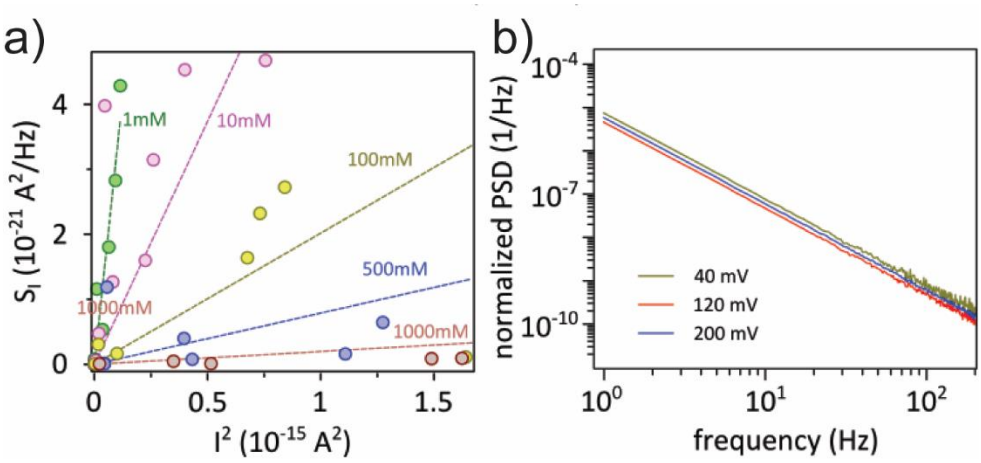

Figure V.11. Noise characterization in interfacial nanopores. a) The distribution of the PSDs of 19 different samples as a function of squared current I^2 : Samples with diverse geometries ($50\ nm \leq h \leq 300\ nm$ and $10\ nm \leq a \leq 70\ nm$) were measured at fixed transmembrane potential (40 mV), but with different KCl concentrations. Dashed lines show the best linear fit for the data of each concentration. b) Normalized power spectral density of an interfacial nanopore ($h = 200\ nm$, $a = 50\ nm$)**,** in low frequency regime and under different transmembrane potentials; the measurements performed with 100 mM KCl. Clearly, the noise in our nanopores did not follow the Hoog's model as if so, one would have expect overlapping of the curves.

V.X References

(1) Lipomi, D. J.; Martinez, R. V; Whitesides, G. M. *Angew. Chem. Int. Ed. Engl.* **2011**, *50* (37), 8566–8583.

(2) Plesa, C.; Dekker, C *Nanotechnol.* **2015**, 26(8), 084003.

(3) Hall, J. R. *J. Gen. Physiol.* **1975**, *66* (2), 531–532.

(4) Wanunu, M.; Dadosh, T.; Ray, V.; Jin, J.; McReynolds, L.; Drndić, M. *Nat. Nanotechnol.* **2010**, *5* (11), 807–814.

(5) Smeets, R. M. M. R. M. M.; Keyser, U. F. U. F.; Krapf, D.; Wu, M. Y. M. Y.; Nynke, H.; Dekker, C.; Dekker, N. H.; Dekker, C. *Nano Lett.* **2006**, *6* (1), 89–95.

(6) He, Y.; Tsutsui, M.; Taniguchi, M.; Kawai, T. *J. Mater. Chem.* **2012**, *22* (27), 13423.

(7) Schneider, G. F.; Kowalczyk, S. W.; Calado, V. E.; Pandraud, G.; Zandbergen, H. W.; Vandersypen, L. M. K.; Dekker, C. *Nano Lett.* **2010**, *10* (8), 3163–3167.

(8) Singer, A.; Rapireddy, S.; Ly, D. H.; Meller, A. *Nano Lett.* **2012**, *12* (3), 1722–1728.

(9) Merchant, C. A.; Healy, K.; Wanunu, M.; Ray, V.; Peterman, N.; Bartel, J.; Fischbein, M. D.; Venta, K.; Luo, Z.; Johnson, A. T. C.; Drndić, M.; et al. *Nano Lett.* **2010**, *10* (8), 2915–2921.

(10) Garaj, S.; Liu, S.; Golovchenko, J. A.; Branton, D. *Proc. Natl. Acad. Sci.* **2013**, *110* (30), 12192–12196.

(11) Siwy, Z.; Fuliński, A. *Phys. Rev. Lett.* **2002**, *89* (15), 158101.

(12) Smeets, R. M. M.; Keyser, U. F.; Wu, M. Y.; Dekker, N. H.; Dekker, C. *Phys. Rev. Lett.* **2006**, *97* (8), 88101.